FSU-HEP-090193

Massive Hadron Pair Production by 800 GeV/c Protons on Nuclear Targets

H.B.White[a], K.Streets[b], G.Boca[c], C.Georgiopoulos,
J.H.Goldman, S.Hagopian, V.Hagopian, K.F.Johnson,
D.Levinthal, F.Lopez[d], H.L.Sawyer[e], J.Streets[a]

Florida State University, Tallahassee, Florida 32306

M.Crisler, A.Lathrop, S.Pordes

Fermi National Accelerator Laboratory, Batavia, Illinois 60510

M.Cummings[f], H.R.Gustafson

University of Michigan, Ann Arbor, Michigan 48109

We report data on proton-nucleon collisions obtained on Fermilab experiment 711, in which high transverse momentum hadrons are produced near 90° in the proton-nucleon center of mass forming high mass states, using an 800 GeV/c proton beam on targets of beryllium, aluminum, iron and tungsten. The data presented covers the mass range from 6 to 15 GeV/c^2, the three di-hadron charge states $++$, $+-$ and $--$, and parton-parton scattering angles up to $\cos\theta^* = 0.50$.

We present the differential mass di-hadron cross-section, as well as the angular and charge dependence of the measurement. The cross-section as a function of the parton-parton scattering angle for the three charge states is shown to vary linearly with the value of the atomic weight. While the angular distributions are shown to be independent of the target type, a small dependence on the charge state of

the distributions is observed. The data are shown to be in good agreement with extrapolations from previous measurements and phenomenological QCD calculations.

PACS numbers: 13.85.Hd, 13.87.Fh

I. INTRODUCTION

High transverse momentum hadronic production has been used to study QCD[1], since its discovery in 1972[2]. The interpretation of data on the production of a single high p_T particle is complicated, however, by effects due to the intrinsic motion of the partons. Data from nuclear targets[3] may be further complicated both by collective nuclear effects on the intrinsic motion of the partons[4], and by interactions of the scattered partons with the nuclear matter. While data on leptonic hadron production from nuclear targets[5] suggest that for leading particles the latter effect is small, experiments using jet-like triggers [6] have found large nuclear effects. However, two particle inclusive reactions, with the two observed secondaries forming a high mass state ($M_{pair} \approx p_{T1}+p_{T2}$), can return the interpretation of the data to a simpler form. In particular, the calculated cross sections are insensitive to the initial state motions incorporated in the models[7]. The present experiment was designed to investigate the hard scattering predictions of QCD in hadronic collisions by observing such high mass di-hadron events in proton-nucleus collisions. We present data taken between November 1987 and February 1988, on the dependence of the cross section with atomic weight (A) for the production of pairs of charged hadrons on four nuclear targets, the di-hadron mass cross sections, and the CM angular and charge dependence of the reaction p + nucleus $\rightarrow H^{\pm}H^{\pm}$ + X, measured by Fermilab experiment 711.

II. EXPERIMENTAL APPARATUS

The experiment was designed to observe high mass charged di-hadron pairs over a large center of mass solid angle in the charge states $+-$, $++$ and $--$. The apparatus is shown in Figure 1 and has been described in detail in two Ph.D dissertations [8]. It was a double arm magnetic spectrometer with a calorimetric trigger. The

two arms of the tracking system were defined by deactivating central horizontal bands of large aperture mini-drift chambers to allow the non-interacting beam and forward jets to pass through unobserved. The two calorimeters were segmented vertically to allow localized energy depositions to be used to estimate the transverse momentum of particles in the trigger. Each calorimeter was supplemented with two vertically segmented hodoscopes to identify the incident particles as charged. The 16 segments of each hodoscope and calorimeter formed a projective geometry to the target.

A. Beam, Targets, and Analyzing Magnets

This experiment was operated within the Neutrino East Beamline (NE). In addition to secondary beams, this beamline also supports primary protons from the accelerator. The general properties of NE include a maximum proton momentum of 900 GeV/c, with a momentum dispersion $\Delta p/p$ of 3.3% and a maximum flux of 5 $\times 10^7$ protons per second per 10^{12} protons extracted from the accelerator [9]. The design and operating conditions expected of the NE beamline were determined by the particle intensity and targeting requirements of the E711 experiment. The design of the horizontal extent of the beam was restricted to be about 1 mm at the E711 target station. This design matches the width of the target in the analyzing magnet bend direction. Thus this constraint provided, as close as feasible, a point origin in one dimension for the interaction vertex in each event. The importance of these thin target and beam size constraints was to maximize the rate capability by eliminating the need for particle tracking instrumentation upstream of the analysis magnets.

Data were taken using four different targets, whose characteristics are presented in Table 1. It should be noted that the z dimension was constrained to be a 10%

interaction length for each target, and the x dimension was fabricated as close to 1mm as possible.

Two analysis magnets just downstream of the target station provided the horizontal magnetic deflection for the spectrometer system. The upstream device, a BM109 magnet, had dimensions of 3.0 meters coil to coil along the beam direction with an aperture size of 50.8 cm in the y direction and 60.9 cm in the x direction. The magnetic length was $\approx$ 2.65 meters in the z direction. The downstream device was a modified 40D48 magnet, with dimensions 1.92 meters long and aperture size 101.6 cm in the y dimension and 93.7 cm in the x dimension. Its magnetic length was $\approx$ 1.78 meters. The magnetic system of the two combined magnets produced a horizontal momentum kick of 1.16 GeV/c.

B. Drift Chambers

The five chambers (in order of their location: DC1, DC2, DC5, DC3, and DC4), were placed downstream of the analysis magnets, and separated along the z-axis so that the corresponding sense wires would symmetrically focus on the target. The chamber locations (z) according to their relative distance to the experimental target and the dimensions (x and y) of the active areas of the chambers as well as other technical information are presented in Table 2.

The chambers were optically surveyed to the beam axis in the designed location. Interactions detected from the target with the magnets powered off were used to align the target to the chambers which were aligned using the energized data. The stack of planes in each chamber included anode planes labeled X, Y, U, and V. The wires in the X, and Y planes were strung vertically and horizontally, respectively, to provide information on the x and y position of the particle's trajectory. The U and V plane wires were oriented 10 degrees clockwise and 10 degrees counter

clockwise of vertical to give additional projected coordinates and to associate the projections when there were more than 1 particle in the spectrometer. The wire spacing in the chambers DC3 and DC4 was large compared to the other chambers. To reduce the drift times, field wires were placed between the anodes and held at positive operating voltages with respect to the sense wires.

The operating voltages of the chambers were set at the low edge of the plateau for the expected flux of high p_T scattered particles in the active regions of the chambers. Consequentially, in the central region, (where the large flux of non-interacting beam particles and low transverse momentum scattered particles traverse the chambers), the ionization produced would be considerably larger. To alleviate this problem, the drift chambers were desensitized in the central beam region. The horizontally oriented cathode wires in this region were operated at a lower voltage than the active regions. This allowed us to operate the experiment at high rates of 2-5 $\times 10^6$ interactions/sec. The plane efficiency was determined by requiring that a track in the spectrometer be recognized by the track reconstruction programs, without using actual data from that plane. The fraction of the time that the plane produced actual data with that requirement was stated as the efficiency. The particle detection efficiency varied over the course of the experiment, so that at the nominal operating conditions the chamber plane efficiency ranged from 78% to 95% over the five chambers.

C. Hodoscopes and Calorimeters

The initial identification of charged particles in the calorimeter was accomplished using a hodoscope consisting of sets of vertically segmented scintillation counters in front of each calorimeter. The hodoscope and calorimeters consisted of two arms vertically separated above and below the beam axis. Each hodoscope

consisted of two planes, HF (front) and HB (back) of 16 separate scintillation counters each, composed of a plate of scintillator 0.93 cm thick, slightly overlapping to eliminate the open spaces between the counters. The dimensions of each module in the hodoscope plane are listed in Table 3.

Each of the calorimeters in this experiment was composed of four sections: the electromagnetic (EM) and three hadronic sections (H1, H2, and H3). Each section in depth, was composed of alternate layers of scintillator and metal. The scintillator layer was further segmented along the y-axis into 16 different modules. Figure 2 illustrates the general structure of these detectors. The EM as well as the H1 sections consisted of 14 layers of 0.635 cm thick scintillator. There were 13 plates of 1.27 cm thick lead for the EM, while H1 used 14 plates of 3.175cm thick steel. Sections H2 and H3 both used 7 plates of 6.35cm thick steel as an absorber with 7 layers of scintillator. The vertical segmentation into 16 modules of scintillator and associated layers of metal, made possible the isolation of energy within a module segment that could be directly associated with a single particle track detected by the drift chambers. The apparatus was designed such that the centers of each corresponding dual hodoscope modules and four calorimeter modules would focus on the target in the vertical direction. The dimensions of the calorimeter modules are also listed in Table 3. The geometric angular acceptance was $\pm$ 25.3 degrees in azimuth (ϕ), and a vertical angle θ_y range of $\pm$ (20 mrad $\rightarrow$ 100 mrad) from the beam axis target location in the laboratory reference frame.

III. DATA ACQUISITION

To trigger on pairs of high p_T hadrons forming high mass states, the approximation ($M_{12} \approx p_{T1} + p_{T2}$) was used. This mass approximation of the hadron pair as the sum of the two particles' transverse momenta is computed to be accurate to

better than 10% for this apparatus. Since the trigger minimum mass was set at 1 GeV below the lowest mass (7.0 GeV) analysis, the turn on efficiency does not affect the trigger in the region of acceptance, and there was no bias in the efficiency as a function of time. In the analysis, the usual analytic method of using four vectors was used in calculating the pair mass. The trigger constructed 12 overlapping sums of the analog signals from 4 adjacent segments for each calorimeter, starting with the second segment from the beam. The gains of the PMTs were adjusted to be proportional to $\sin\theta_y$, thereby making the analog sums approximately proportional to the transverse energy, given the restricted azimuthal coverage ($\pm$ 23.5°). The presence of a single high p_T charged particle incident on one of the calorimeters was established by the coincidence of the two hodoscope signals with a minimum E $\sin\theta_y$ ($\approx p_T$) of 2 GeV/c in the corresponding region of the calorimeter.

A. Trigger

To achieve a simple trigger, 24 "mass" signals were made by adding each of the 24 single particle sums to the total transverse energy detected in the opposite calorimeter, making a "particle-jet" mass. The trigger then required the coincidence of two "mass" signals of greater than 6 GeV/c^2 (one from each side) in coincidence with the two corresponding single high p_T particle signals just described. To improve the experiment live time for some of the running, a higher mass threshold of 12 GeV/c^2 was applied, while the 6 GeV/c^2 mass trigger was prescaled. The trigger efficiency was monitored continuously by means of a prescaled, lower mass threshold trigger. The trigger efficiency was independent of time and the deduced corrections have been applied to the presented data. The additional systematic uncertainty introduced by this correction is estimated as 15% at 6.25 GeV/c^2, 5% at 6.75 GeV/c^2, and negligible for higher masses.

The primary data reduction was done on the FSU ETA-10 supercomputer[10]. The subsequent event selection required that each event satisfy the inclusive requirements of two reconstructed tracks incident on the calorimeter fiducial volumes, forming a vertex, from the non-bend projection, within the target. The two tracks by themselves had to satisfy the trigger requirements and be consistent with the calorimeter pulse height information and latched discriminator signals. The track momentum was calculated by a single bend plane approximation assuming a point source at the center of the target. The chamber resolutions and the finite target size combined to yield a momentum resolution of $\Delta P/P = 2.5 \times 10^{-4}$ P (in GeV/c). This was verified by superimposing Monte Carlo generated tracks (including measured efficiencies and resolutions) onto observed events. The resolution function, including the non-Gaussian tails found in the Monte Carlo studies, caused a negligible distortion of the spectrum over the observed mass range. The systematic uncertainty on the momentum scale was estimated as 2%.

The luminosity was determined by an ion chamber, which measured the total beam flux, and four sets of 90° scintillator telescopes placed symmetrically about the target, used to establish the fraction of the beam incident on the thin target ($\approx$ 90% through the run). The ion chamber was calibrated by scintillation counters in the beam at low intensity (10^5/sec) on two occasions. The uncertainty of the ion chamber calibration over the course of the run was estimated to be less than 2%[8]. Run to run variations of the luminosity monitor calibration were less than 4% for the Be target and less than 2% for the Al, Fe and W targets. The overall normalization error from the ion chamber calibration and the targeting fraction measurement for the data sample was estimated to be 5%. The luminosity measurement was previously reported by this experiment.[11]

The event reconstruction efficiency was evaluated both by use of Monte Carlo

simulated data and by comparison with data reconstructed by a second, independent program. The Monte Carlo simulation explicitly included the inactive sense wires, since they accounted for approximately half of the measured chamber inefficiency. As the operating conditions of the chambers varied over the course of the run, the reconstruction efficiency had to be evaluated for each set of conditions. The analysis of the second reconstruction program confirmed the reconstruction efficiency deduced from the Monte Carlo studies. The reconstruction efficiencies for pairs of tracks (i.e. events) varied from 1.0 for 20 hits tracks to between 0.585 to 0.643 for 16 hit tracks with a systematic error of 8%. The overall event reconstruction efficiency was 0.85 ± 0.07 and independent of variables A, mass, p_T, etc.

The background due to sources other than the target was measured by taking data with the target removed. A special check of the target vertex position was computed by extrapolating the charged tracks. A profile of the reconstructed events at the target produced a gaussian distribution in the non-bend plane with a width corresponding to 0.5 cm and a background of 1-2% from the target holder. The corrections (including interactions in air) were less than 3% for all the targets and has been subtracted from the data. Other backgrounds were estimated to be negligible[8].

B. Acceptance

The acceptance calculation was based on a full event simulation to include the effects of shower containment as well as the geometrical acceptance of the detector. The shower simulation was parameterized using the energy deposition functions determined by CDF[12], which were found to also describe our test beam data. In addition, the simulation made use of the vector capabilities of the supercomputers at FSU[13]. The six dimensional phase-space of the data was analyzed in the following

variables: the mass of the di-hadron system (M_{pair}); its transverse momentum ($\vec{p}_T$; 2 variables); its rapidity in the p-nucleon center of mass (Y_{PN}); the cosine of the polar angle between the di-hadron axis and the beam direction in the rest frame of the massive state ($\cos\theta^*$); and the azimuthal angle of the plane defined by the beam direction and the di-hadron axis in that frame (ϕ^*). To describe the data accurately, the components of the transverse momentum of the massive state in the plane of the scattering and perpendicular to this plane required different parameterizations. The perpendicular component could be described by a Gaussian while the parallel component was described by a polynomial. We interpret this as the combined effect of the parton "Fermi" motion and the jet fragmentation.

Acceptance maps, calculated from the simulated events, for each charged state were defined in four of the variables (M_{pair}, Y_{PN}, $\cos\theta^*$, $|\ p_{T_{pair}}\ |$), integrating over the other two ($\hat{p}_T$, ϕ^*). The fiducial volume cut was determined by finding stable agreement between the actual event distributions and the simulated distributions, which explicitly included corrections for the inefficiency introduced by the existence of inactive chamber sense wires. This implies a dependence of the reconstruction efficiency on the location within the 6 dimensional phase space. To account for this effect, efficiency maps were calculated in two of the variables (Y_{PN}, $\cos\theta^*$) for the three charge states individually in each of the mass bins. These efficiency maps were also used in the calculation of the event by event weights. The acceptance maps were used as lookup tables to determine weights on an event by event basis. A graphical representation of the acceptance correction for one table with a $p_{T_{pair}}$, limit of 2.0 GeV/c, in the mass bin of 9.0-10.0 GeV/c^2 , with a cosine of the scattering angle and rapidity bin size of 0.05, is shown in Figure 3. This illustrated acceptance correction table was used for unlike sign di-hadron events. The major contribution to this inefficiency is due to the azimuthal acceptance of 24.8% which is unbiased.

For the cross section calculations the events were limited to $|\cos\theta| < 0.25$ insuring maximal efficiency essentially equal to the azimuthal acceptance. The geometric azimuthal acceptance was calculated to better than 1% and the overall acceptance was accurate to 3%.

IV. RESULTS

To insure complete shower containment in the calorimeter the mass cross sections are defined as the integral over a restricted region of phase-space given by $-0.4 < Y_{PN} < 0.2$, $|\cos\theta^*| < 0.25$, $M_{pair} > 6$ GeV/c^2 and either $|p_{T_{pair}}| < 1$ GeV/c or $|p_{T_{pair}}| < 2$ GeV/c. The mass cross section is then defined as:

$$\left.\frac{d\sigma}{dM_{pair}dY_{PN}}\right|_{Y\approx 0} \equiv \frac{1}{\Delta Y_{PN}} \cdot \int dp_{T_{pair}} \int d\cos\theta^* \int \frac{d\sigma}{dM_{pair}dY_{PN}d\cos\theta^* dp_{T_{pair}}}$$

The dependence of the event yield per unit luminosity on atomic weight has been parameterized in the form $\ln[\sigma(A)] = \alpha \ln A + \ln\sigma_0$, for each di-hadron mass range and charge state, a $p_{T_{pair}}$ range and over the range of the parton-parton scattering angle. The results of the fits for a as a function of mass for the three different charge states, two $p_{T_{pair}}$ ranges ($p_{T_{pair}} < 1$ GeV/c) and ($p_{T_{pair}} < 2$ GeV/c), but over a limited range of $\cos\theta^* < 0.2$ was reported previously by this experiment[11]. The average values reported for $p_{T_{pair}} < 1$ and < 2 GeV/c were 1.043 ± 0.011 and 1.049 ± 0.007 respectively, with an average systematic error in α of 0.025. In the current analysis using a less restricted range of the parton-parton scattering angle $|\cos\theta^*| < 0.5$, the results of the fits for a are consistent with the above results in the restricted angular range and $p_{T_{pair}}$ range. With the larger extracted data sample, the average value of α over the larger $\cos\theta^*$ range is 1.018 ± 0.009 with a systematic error of 0.035. The numerical values and their statistical errors for α are presented in Table 4. The results for α vs. $\cos\theta^*$ are also shown for the three charge states

in Figure 4.

Another hadron pair production experiment studied the charge state H^+H^- with high statistics[14]. For comparison to our experiment, the 8 to 10 GeV/c^2 data from that experiment was extrapolated to 7.25 GeV/c^2, and the atomic weight dependence parameter α was calculated from their W to Be ratio to be 1.04. An α of 1.04 is consistent with the value of 1.043$\pm$0.011 measured in our experiment. At values above 7.5 GeV/c^2, we are within one (1) standard deviation of the results of reference 14.

To compare these data with the predictions of QCD/parton model calculations, the cross sections have been evaluated per nucleon. As the atomic weight dependence of the cross sections has been found to be consistent with the form $\sigma(A) = \sigma_0 A^{1.0}$, we have extracted the average cross sections per nucleon assuming a linear atomic weight dependence. The overall systematic uncertainty of the normalization is 28% at 6.0 GeV/c^2, 18% at 6.5 GeV/c^2, and 13% for the higher masses. The systematic error in the mass scale is 2%.

The cross sections for massive di-hadron production per nucleon for the 3 charge states are shown in Figures 5 and 6 for $p_{T_{pair}} < 1$ and $p_{T_{pair}} < 2$ GeV/c respectively with numerical values listed in Tables 5 and 6. Also shown is the empirical function found from the CCOR $\pi^0\pi^0$ data[15], corrected for the different integration ranges. The CCOR function is approximately a factor of two lower than the +− data. We attribute this to the difference in the charge states. The factor of two can be accounted for if the fragmentation function into π^0's is equal to the geometric mean of the fragmentation functions into π^+ and π^-, as there are two configurations for the +− state. The CCOR data have been shown to be consistent with phenomenological QCD calculations[7],[16].

The major systematic uncertainties in the shape of the $\cos\theta^*$ distribution arise

from the nonuniformity of the magnetic field and the uncertainty in the acceptance corrections. The nonuniform field causes a momentum scale error that varies with position. While the field irregularities are estimated to be less than 1%, the steep cross section turns this into a 10% relative error as $\cos\theta^*$ is varied. The uncertainty in the acceptance is believed to be 10% at the largest value of $\cos\theta^*$ (0.50). The total systematic uncertainty is therefore stated as 16% in the relative normalization over the variation in $\cos\theta^*$.

The phase space projection onto $\cos\theta^*$ should maximize the data sample without distorting the distribution. To maximize the range in $\cos\theta^*$ the rapidity interval integrated over must be limited such that all values of $\cos\theta^*$ have reasonable acceptance. This avoids the rapidity integration distorting the angular distribution, through systematic errors in the acceptance. For the angular distribution analysis of the experiment, the rapidity range was defined by $-0.25 < Y_{PN} < 0.1$. To limit the variations in the choice of definition in $\cos\theta^*$, the transverse momentum of the massive state $p_{T_{pair}}$, was required to be less than 2 GeV/c. The distributions in $\cos\theta^*$, normalized by the total integrated cross section, are shown for $7.0 < M_{pair} < 7.5$ GeV/c^2, and 7.5 GeV/$c^2 < M_{pair}$, in Figure 7 for the three charge states.

The mass distributions can be compared with the expectations of the QCD/parton model. To investigate this, we have taken the Monte Carlo calculation of reference 15. After correcting an error (a factor of $(2X_1X_2)^{-1}$), using newly derived structure functions[17], and normalized, scale violating[18] fragmentation functions[19] extracted from EMC data[20], we optimized the choice of Q^2 for agreement with the CCOR[15] data. The results of the calculation of the mass cross sections, the cross sections from CCOR[15] and this experiment are shown in Figure 8 (with various additional factors of ten to separate the samples) as a function of mass state and $\sqrt{S}$. The data from this experiment is in the charge states

++, +−, −−, while the CCOR data is from π^0 pairs. We consider the agreement to the current experiment excellent, as the calculation was only adjusted (choice of Q^2) to the CCOR data.

To study the angular distributions, the data from this experiment and CCOR were fit to the symmetrized form:

$$\frac{1}{2}\left[\frac{1}{(1+\cos\theta^*)^{\mathbf{a}}}+\frac{1}{(1-\cos\theta^*)^{\mathbf{a}}}\right]$$

The results of the fit to our data yielded a power "**a**" effectively independent of the target type and with a small variation over the two mass bins but with nearly all the same sign fits yielding consistently higher values. The value for this parameter for a fit to all the accumulative opposite sign and same sign data yielded powers "**a**" of 3.01± 0.04 and 3.30 ± 0.07 respectively. Truncating the $\cos\theta^*$ range to limit the systematic uncertainty of the acceptance has a negligible effect.

A QCD Monte Carlo calculation could also be fit to the above form. Table 7 lists the values of the fit parameter a obtained from fits of this form to the normalized experimental data and QCD Monte Carlo generated data. The results from the CCOR experiment, and the current experiment are shown in Figure 9 as a function of mass state and scattering angle. The values found from the Monte Carlo calculation are on average consistent with the low mass state data of the current experiment and the CCOR results, but consistently smaller than the (lower statistics) high mass state data. The measured angular distributions are a weighted average over the angular distributions of various subprocesses, such as gluon-valence quark (gq-gq), and gluon-gluon (gg-gg, gg-qq) scattering as well as the process valence quark-valence quark (qq-qq) scattering. The distributions from these processes have nearly the same shape, and therefore their contributions can not be separately

measured. The difference in the charge states (as exemplified by the shape parameter of the angular distribution), if real, may be due to the difference in the angular dependence of the matrix elements between same and unlike type quark scattering. The same type quark scattering is affected by the interference of two Feynman diagrams while the unlike type scattering is not. While the statistical significance of the experimental charge difference is small, it is certainly suggestive.

We would like to thank the National Science Foundation and the U.S. Department of Energy for funding this work. The experiment would not have been possible without the fine technical support of Fermilab and Florida State University. We especially extend our thanks to the following persons who took part in the construction, operational support, and early testing: B.Baller, M.Bertoldi, D.Kaplan, T.Kramer, S.Ploplys and J.Volk. We also express gratitude to J. Owens for his help in the theoretical interpretation of the data.

REFERENCES

[a] Present address: Fermi National Accelerator Laboratory, Batavia, Illinois 60510

[b] Present address: University of Maryland, College Park, Maryland 20742

[c] Present address: University of Pavia, Sezione INFN, Pavia, Italy

[d] Present address: Argonne National Laboratory, Argonne, Illinois 60439.

[e] Present address: University of Texas Arlington, Arlington, Texas 76019

[f] Present address: University of Hawaii, Honolulu, HI 96822.

[1] S. Berman, J. D. Bjorken, and J. Kogut, Phys. Rev. **D4**, 3388 (1971).

[2] B. Alper et al., Phys. Lett. **44B**, 521 (1973). F. W. Büsser et al., Phys. Lett. **46B**, 471 (1973).

[3] J.W.Cronin et al., Phys. Rev. D **11** 3105 (1975).

[4] A.Bodek, J.L.Ritchie, Phys. Rev. D **23**,1070 (1981), and **24**, 1400 (1981). J.J.Aubert et al., Phys. Lett. **123B**, 275 (1983).

[5] A.Arvidson et al., Nucl. Phys. **B246**, 381 (1984).

[6] H.E.Miettinen, Nucl.Phys. **A418**,315 (1984). R.Gomez et.al., Phys. Rev. D **35**, 2736 (1987).

[7] J.Owens, Phys. Rev. D **20**, 221 (1979). R.Baier, J.Engels and B.Petersson, Z. Phys. C **2**, 265 (1979).

[8] K. R. T. Streets, The Atomic Weight Dependence and Mass Cross Sections of

Massive Hadron Pair Production In Proton-Nucleus Collisions at 800 GeV/c; Ph.D. dissertation, Florida State University, (1989), unpublished. H. B. White, A Study of Angular Dependence in Parton-Parton Scattering From Massive Hadron Pair Production; Ph.D. dissertation, Florida State University (1991), unpublished.

[9] Current Experiments in Elementary Particle Physics, Univ. of California **LBL-91** Revised ,Fermilab Beams (Source: H. B. White, Jr), 173 (September 1989).

[10] C. H. Georgiopoulos, J.H.Goldman, M.Hodous, Nucl. Instr. and Methods **A261**, 493 (1987).

[11] K. Streets et al., Phys. Rev. Lett. **66**,864 (1991).

[12] J.Freeman and A.Beretvas, *Proceedings of the 1986 Summer Study on the Physics of the Superconducting Supercollider*, ed. by R. Donaldson and J. Marx (APS, 1986), p. 482.

[13] D. Levinthal et al., Computer Physics Comm. **45**, 137 (1987). D.Levinthal, *Proceedings of the CERN Summer School of Computing,* ed. by C. Verkerk, (CERN, Geneva, 1988), CERN-88-3, p. 223.

[14] P. B. Straub et al., Phys. Rev. Lett. **68**, 452 (1992).

[15] A.L.S. Angelis et al., Nucl. Phys. **B209**, 284 (1982).

[16] J. F. Owens, Rev. Mod. Phys. **59**, 465 (1987) . M. Jacob, Proc. EPS Int. Conf. on High Energy Physics, Geneva, 1979 (CERN, Geneva, 1980), p. 473.

[17] D. W. Duke and J. F. Owens, Phys. Rev. **D30**, 49 (1984).

[18] D. J. Gross Phys. Rev. Lett. **32**, 1071 (1974).

[19] J. F. Owens, E. Reya, and M. Glück, Phys. Rev. **D18**, 1501 (1978). J. F.Owens Phys. Rev. **D19**, 3279 (1979).

[20] M. Arneodo et al., Nucl. Phys. **B**. (1989).

Table 1. Technical Information on the Experimental Targets

Target Material	Atomic Weight	Dimensions			% Interaction Length
		x (cm)	y (cm)	z (cm)	
Beryllium	9.01	0.10225	5.715	4.066	9.99
Aluminum	26.98	0.08357	5.715	3.951	10.03
Iron	55.85	0.08492	5.715	1.670	9.97
Tungsten	183.85	0.10211	5.715	0.956	9.97

Table 2. Parameters of the Drift Chambers

Chamber	Active Region		Distance to Target	Wires Spacing				Number of sense wires
	x(cm)	y(cm)	z (cm)	Anode	Cathode	Field	Ground	
				(mm)				
DC1								
X, Y	103.9	110.4	539.0	2.03	1.0	—	2.0	256, 544
U, V	103.9	110.4	539.0	2.03	1.0	—	2.0	320, 320
DC2								
X, Y	129.5	137.6	675.0	2.53	1.0	—	2.0	256, 544
U, V	129.5	137.6	675.0	2.53	1.0	—	2.0	320, 320
DC5								
X, Y	169.3	175.7	823.0	3.05	2.0	—	2.0	256, 576
U, V	169.3	175.7	823.0	3.05	2.0	—	2.0	352, 352
DC3				—	—	—	—	
X, Y	224.7	226.8	1118.0	4.17	2.0	4.17	2.0	256, 544
U, V	224.7	226.8	1118.0	4.11	2.0	4.11	2.0	352, 352
DC4				—	—			
X, Y	299.1	302.5	1486.0	5.56	2.0	5.56	2.0	256, 544
U, V	299.1	302.5	1486.0	5.47	2.0	5.47	2.0	352, 352

Table 3. Parameters of the Hodoscope and Calorimeter
Scintillator thickness shown as the value of z

Module number	Hodoscope		Calorimeter			
			EM and H1		H2 and H3	
	X and Y		X	Y	X	Y
	(z= 0.93 cm)		(z= 0.635 cm)		(z= 0.635 cm)	
	(cm)	(cm)	(cm)	(cm)	(cm)	(cm)
1	29.5	6.35	44.7	5.1	49.0	5.1
2	33.8	6.35	49.0	5.1	53.3	5.1
3	38.1	6.35	53.3	5.1	57.4	5.1
4	42.2	6.35	57.4	5.1	61.7	5.1
5	46.5	6.35	61.7	5.1	66.0	5.1
6	52.8	8.89	68.1	7.6	74.4	7.6
7	59.2	8.89	74.4	7.6	81.0	7.6
8	65.8	8.89	81.0	7.6	87.4	7.6
9	72.1	8.89	87.4	7.6	97.8	12.7
10	82.6	14.0	97.8	12.7	108.5	12.7
11	93.2	14.0	108.5	12.7	119.1	12.7
12	103.9	14.0	119.1	12.7	129.5	12.7
13	114.3	14.0	129.5	12.7	140.2	12.7
14	125.0	14.0	140.2	12.7	150.9	12.7
15	134.6	14.0	150.9	12.7	161.5	12.7
16	146.3	14.0	161.5	12.7	172.0	12.7

Table 4. Atomic weight dependence parameter α , as a function of the parton-parton scattering angle for $p_{T,pair} < 2.0$ GeV/c.

Mass (GeV/c^2)	$\cos\theta^*$ (bin center)	H^-H^-	H^+H^-	H^+H^+
$7.0 < M_{pair} < 7.5$	0.025	0.88 ± 0.03	0.97 ± 0.01	1.01 ± 0.01
	0.075	0.97 ± 0.03	0.98 ± 0.02	1.06 ± 0.02
	0.125	0.99 ± 0.04	0.98 ± 0.02	0.93 ± 0.02
	0.175	0.87 ± 0.04	0.96 ± 0.03	1.08 ± 0.03
	0.225	0.85 ± 0.05	0.94 ± 0.03	1.02 ± 0.03
	0.275	1.04 ± 0.08	0.97 ± 0.04	1.02 ± 0.03
	0.325	1.09 ± 0.09	0.89 ± 0.04	0.93 ± 0.03
	0.375	1.08 ± 0.09	0.96 ± 0.03	1.09 ± 0.05
	0.425	1.01 ± 0.10	0.95 ± 0.04	0.96 ± 0.04
	0.475	0.99 ± 0.09	0.88 ± 0.04	0.98 ± 0.04
$7.5 < M_{pair}$	0.025	1.03 ± 0.06	1.17 ± 0.03	1.14 ± 0.03
	0.075	1.03 ± 0.11	1.05 ± 0.04	1.20 ± 0.03
	0.125	1.11 ± 0.10	1.07 ± 0.05	1.07 ± 0.05
	0.175	1.15 ± 0.16	1.07 ± 0.05	1.06 ± 0.05
	0.225	0.91 ± 0.17	1.06 ± 0.06	1.13 ± 0.08
	0.275	1.03 ± 0.25	1.00 ± 0.08	1.07 ± 0.09
	0.325	0.99 ± 0.24	1.03 ± 0.08	1.19 ± 0.08
	0.375	1.04 ± 0.28	0.93 ± 0.08	1.02 ± 0.14
	0.425	0.91 ± 0.27	1.01 ± 0.09	0.98 ± 0.10
	0.475	1.17 ± 0.26	0.89 ± 0.07	1.02 ± 0.10

Table 5. $\frac{d\sigma}{dMdY}$ per nucleon for $p_{T,pair} < 1$ GeV/c di-hadron data in nanobarns/GeV/c^2. The errors shown are statistical.

Mass (GeV/c^2)	H^-H^-	H^+H^-	H^+H^+
6.25	1.786 ± 0.079	3.330 ± 0.056	2.616 ± 0.094
6.75	0.803 ± 0.047	1.476 ± 0.033	1.437 ± 0.063
7.25	0.312 ± 0.024	0.683 ± 0.021	0.615 ± 0.033
7.75	0.141 ± 0.014	0.334 ± 0.013	0.261 ± 0.019
8.25	0.0593 ± 0.0082	0.1686 ± 0.0094	0.124 ± 0.012
8.75	0.0332 ± 0.0062	0.0986 ± 0.0072	0.0589 ± 0.0082
9.25	0.0195 ± 0.0045	0.0496 ± 0.0051	0.0441 ± 0.0067
9.75	0.0113 ± 0.0034	0.0239 ± 0.0035	0.0172 ± 0.0041
10.5	0.0027 ± 0.0011	0.0146 ± 0.0019	0.0158 ± 0.0027
11.5	—	0.0058 ± 0.0012	0.0044 ± 0.0014
12.5	0.0007 ± 0.0005	0.0015 ± 0.0006	0.0012 ± 0.0006
13.5	—	0.0005 ± 0.0003	—
14.5	—	0.0004 ± 0.0003	—

Table 6. $\frac{d\sigma}{dMdY}$ per nucleon for $p_{T,pair} < 2$ GeV/c di-hadron data in nanobarns/GeV/c^2. The errors shown are statistical.

Mass (GeV/c^2)	H^-H^-	H^+H^-	H^+H^+
6.25	4.62 ± 0.12	8.928 ± 0.098	7.97 ± 0.16
6.75	2.028 ± 0.073	4.201 ± 0.061	4.18 ± 0.10
7.25	0.801 ± 0.038	1.952 ± 0.038	1.718 ± 0.055
7.75	0.381 ± 0.023	0.937 ± 0.024	0.750 ± 0.033
8.25	0.191 ± 0.015	0.470 ± 0.017	0.333 ± 0.020
8.75	0.089 ± 0.010	0.269 ± 0.013	0.212 ± 0.016
9.25	0.0453 ± 0.0069	0.1341 ± 0.0087	0.121 ± 0.011
9.75	0.0278 ± 0.0054	0.0793 ± 0.0067	0.0760 ± 0.0088
10.5	0.0094 ± 0.0021	0.0405 ± 0.0033	0.0381 ± 0.0042
11.5	0.0023 ± 0.0010	0.0141 ± 0.0020	0.0156 ± 0.0027
12.5	0.0011 ± 0.0006	0.0061 ± 0.0012	0.0040 ± 0.0012
13.5	—	0.0008 ± 0.0004	0.0020 ± 0.0008
14.5	—	0.0008 ± 0.0004	0.0002 ± 0.0002

Table 7. Values of the parameter a obtained from fits to the QCD Monte Carlo calculations, and fits to the experimental data are listed.

Target Type	H^-H^-	H^+H^-	H^+H^+	
	Mass Range $7.0 < M_{pair} < 7.5$ (GeV/c^2)			
Beryllium	**2.61 ± 0.26**	**2.83 ± 0.10**	**3.06 ± 0.17**	
	2.88 ± 0.03	2.87 ± 0.03	2.89 ± 0.03	← QCD
Aluminum	**2.52 ± 0.28**	**2.72 ± 0.12**	**2.67 ± 0.19**	
	2.88 ± 0.03	2.87 ± 0.03	2.89 ± 0.03	← QCD
Iron	**2.72 ± 0.22**	**2.90 ± 0.09**	**2.83 ± 0.14**	
	2.85 ± 0.03	2.88 ± 0.03	2.89 ± 0.03	← QCD
Tungsten	**3.64 ± 0.34**	**2.63 ± 0.16**	**3.12 ± 0.24**	
	2.85 ± 0.03	2.83 ± 0.03	2.85 ± 0.03	← QCD
Integrated Target data	**2.73 ± 0.13**	**2.82 ± 0.05**	**2.87 ± 0.09**	
	Mass Range $7.5 < M_{pair}$ (GeV/c^2)			
Beryllium	**3.83 ± 0.37**	**3.82 ± 0.16**	**3.69 ± 0.26**	
	2.73 ± 0.03	2.76 ± 0.03	2.75 ± 0.03	← QCD
Aluminum	**3.79 ± 0.42**	**2.87 ± 0.20**	**4.87 ± 0.36**	
	2.74 ± 0.03	2.76 ± 0.03	2.75 ± 0.03	← QCD
Iron	**3.42 ± 0.34**	**3.15 ± 0.14**	**3.50 ± 0.22**	
	2.88 ± 0.03	2.88 ± 0.03	2.75 ± 0.03	← QCD
Tungsten	**5.54 ± 0.70**	**3.46 ± 0.26**	**4.04 ± 0.42**	
	2.88 ± 0.03	2.87 ± 0.03	2.89 ± 0.03	← QCD
Integrated Target data	**3.76 ± 0.21**	**3.33 ± 0.09**	**3.81 ± 0.14**	

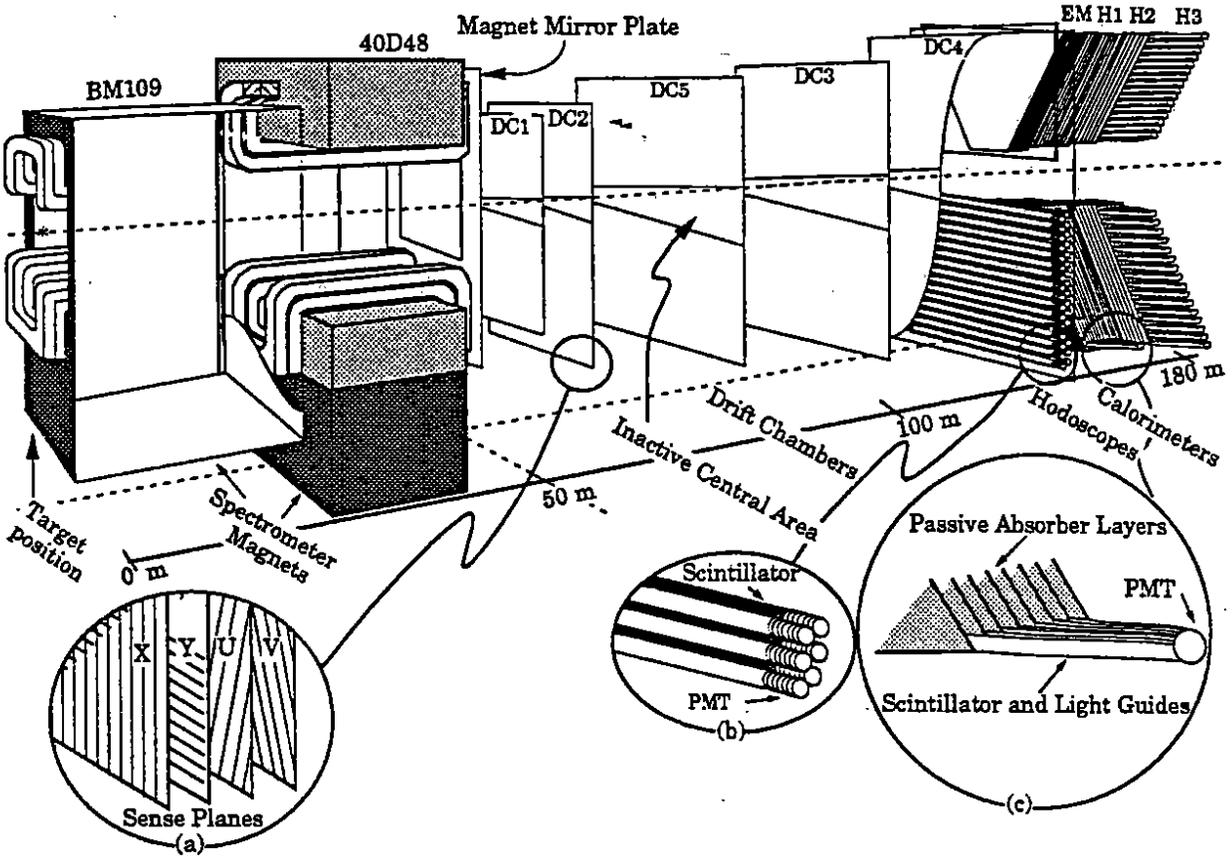

Fig. 1. Schematic view of the Experiment, showing details of the (a) Drift Chambers, (b) Hodoscope, and (c) Calorimeters.

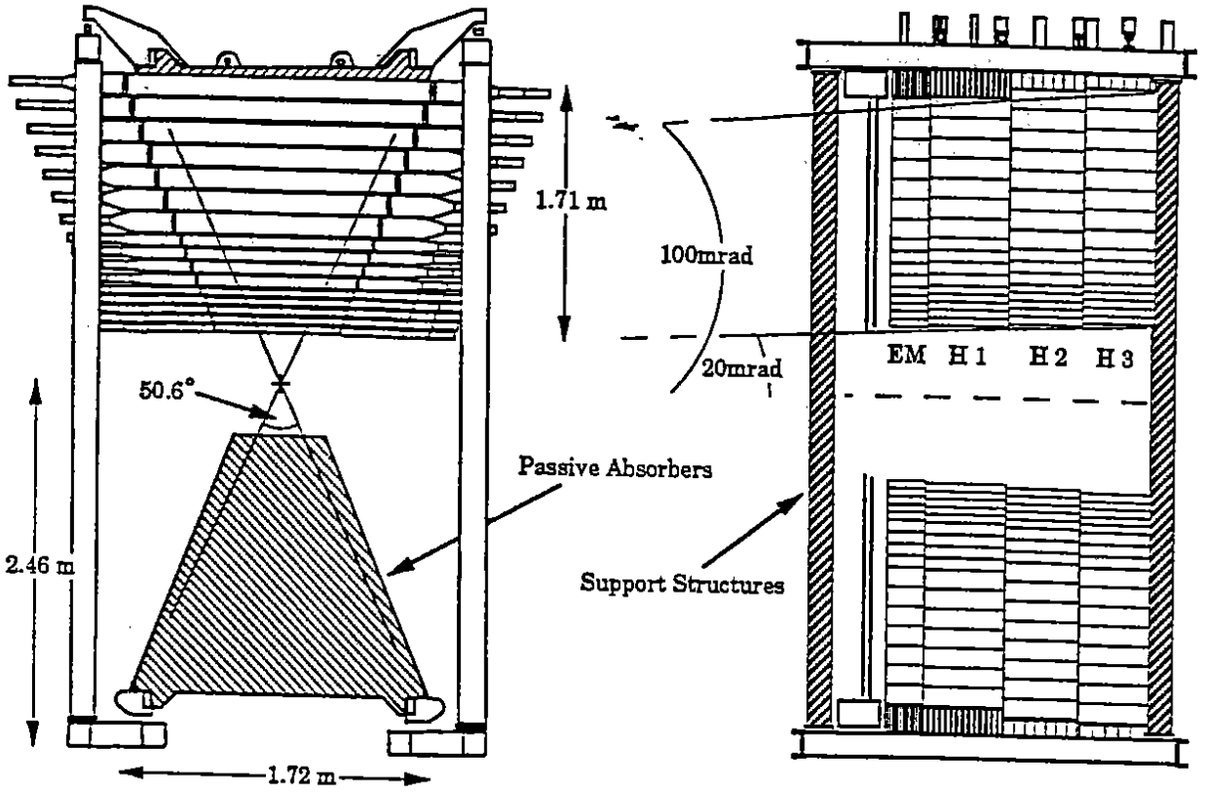

Fig. 2. Front and side views of the calorimeter system.

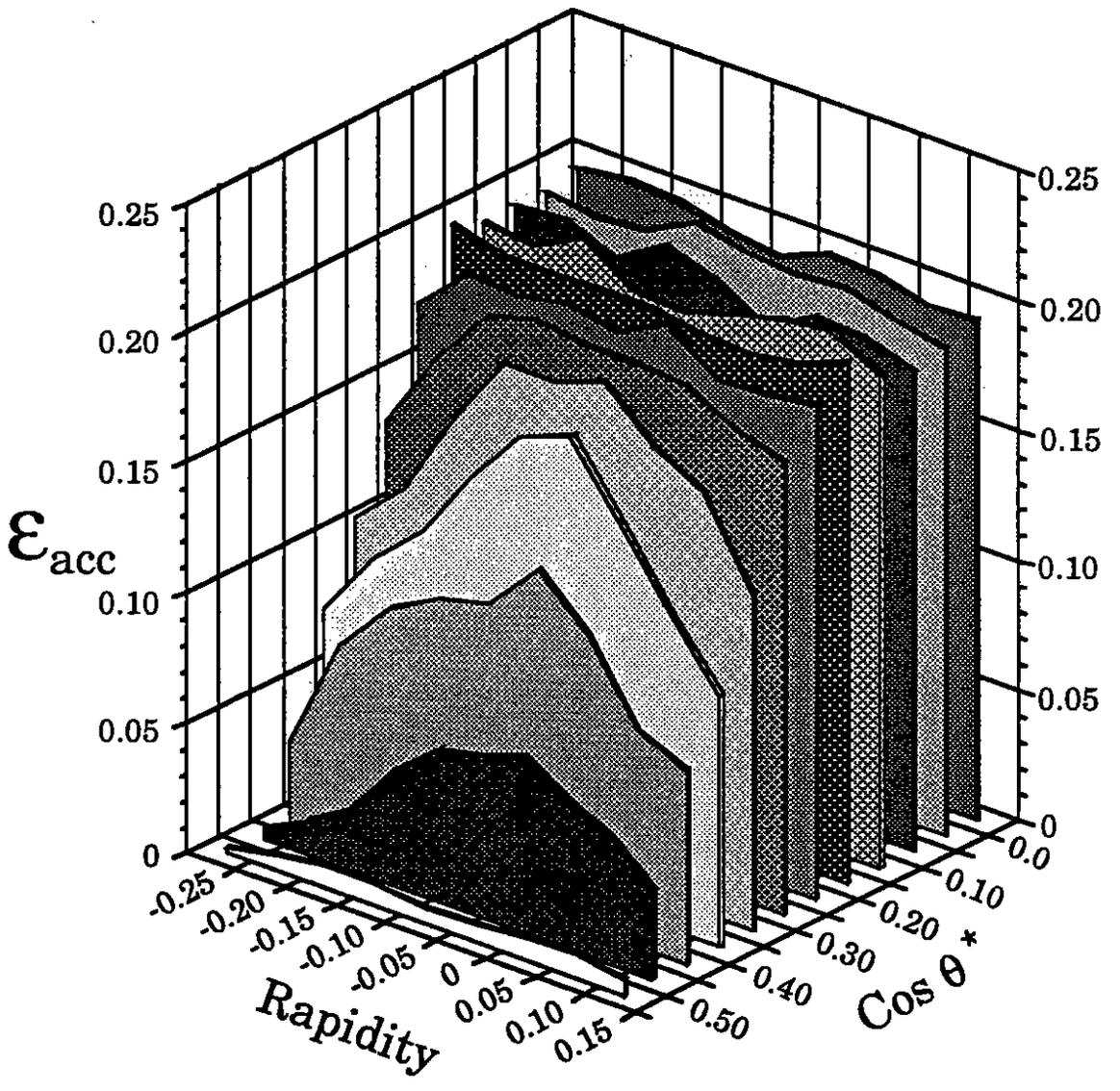

Fig. 3. A graphical representation of one table of the acceptance calculation at a p_T limit of 2.0 Gev/c, in the mass bin of 9.0-10.0 GeV/c^2, with a cosine of the scattering angle and the rapidity bin size of 0.05. This acceptance correction table was used for unlike sign dihadron events.

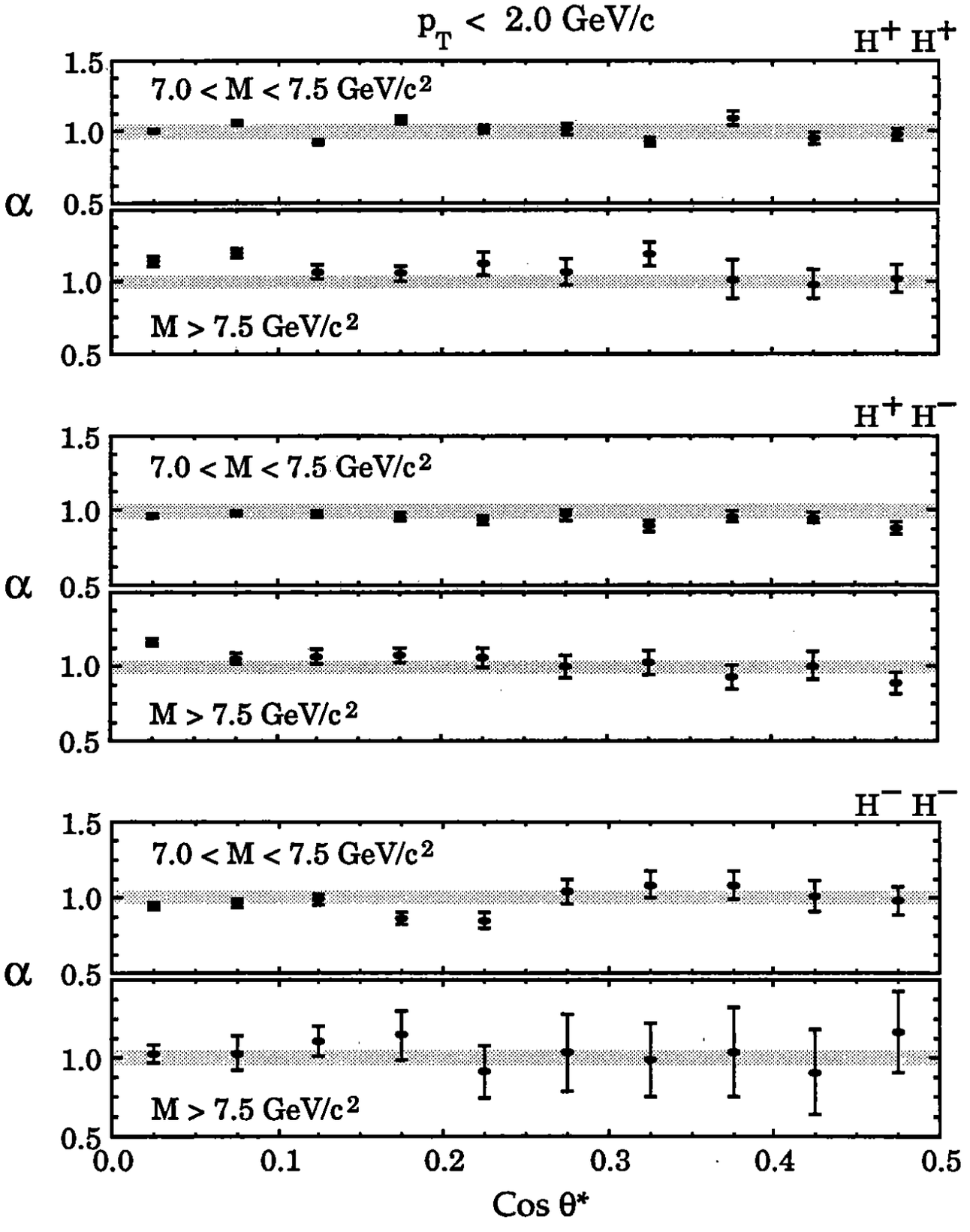

Fig. 4. The atomic weight dependence parameter α is plotted verses the parton-parton scattering angle for the three charge states. For reference, the value of $\alpha = 1.0$ is indicated by the shaded area with a width equal to the error in the global average of all the data values.

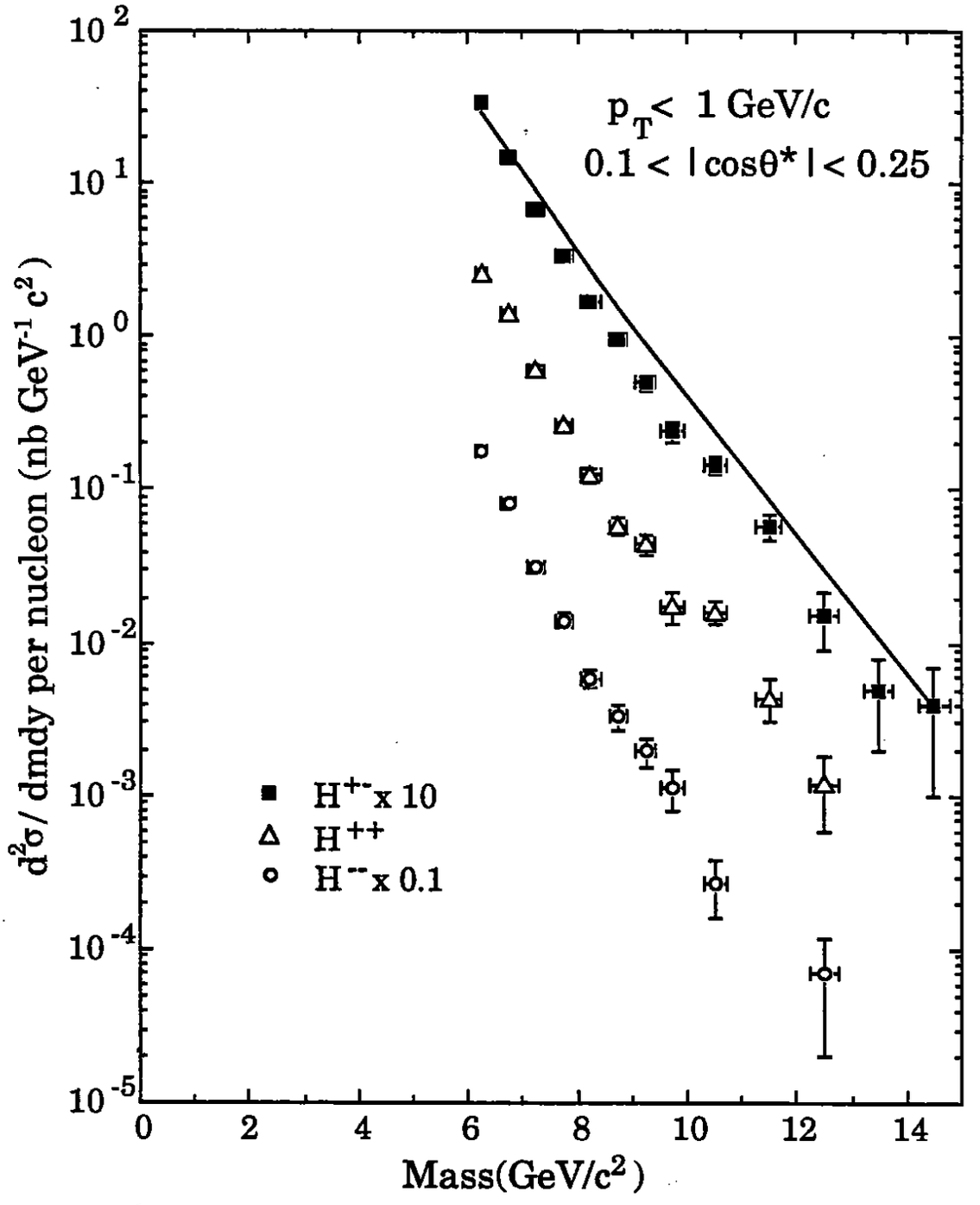

Fig. 5. The differential mass cross section of dihadrons is plotted for $p_T < 1$ GeV/c. H^+ and H^- refer to positive and negative hadrons. The $(+-)$ charge state results and the $(--)$ charge state results have been scaled by the factors indicated for clarity. The curve is the CCOR function.

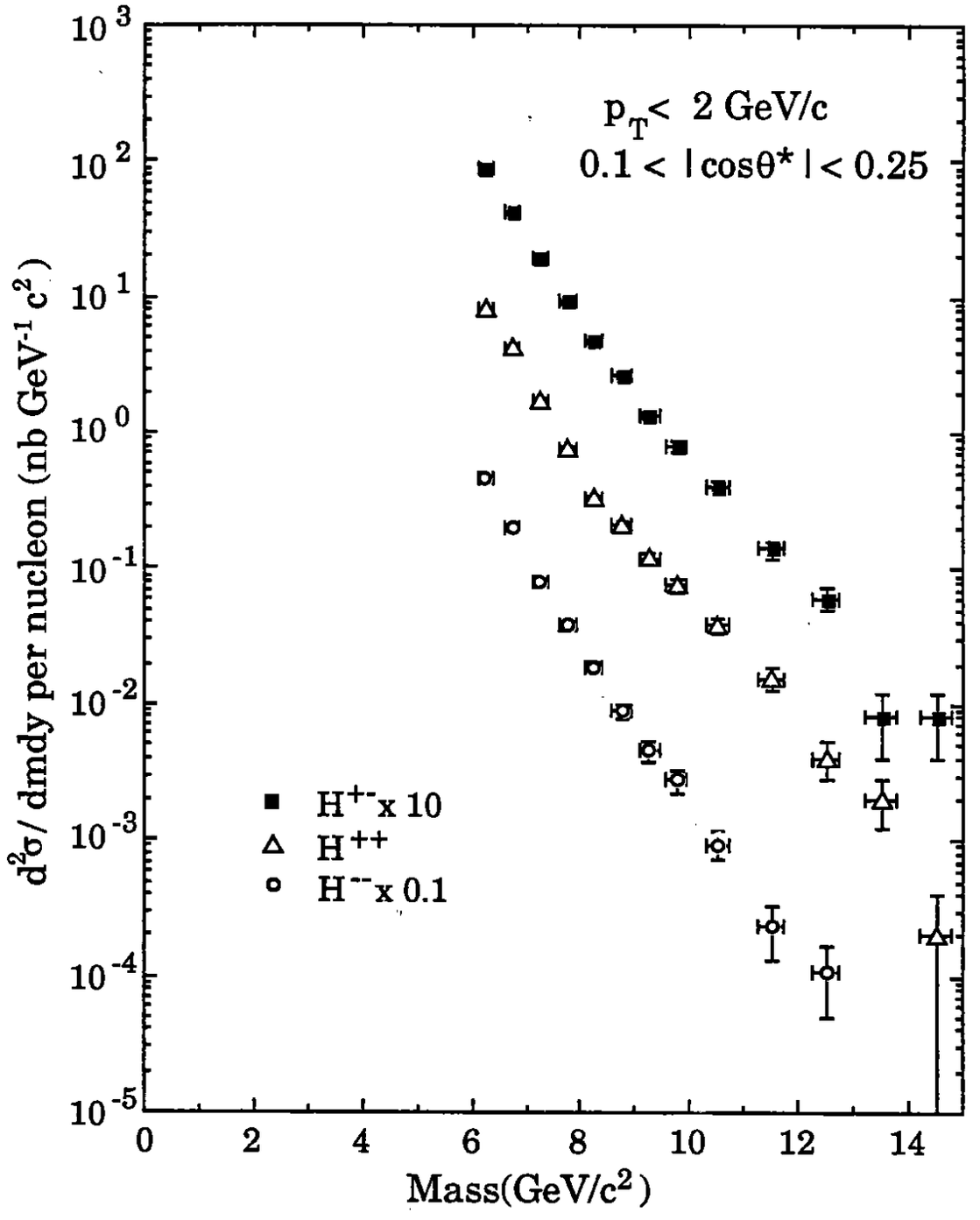

Fig. 6. The differential mass cross section of dihadrons is plotted for $p_T < 2$ GeV/c. H^+ and H^- refer to positive and negative hadrons. The $(+-)$ charge state results and the $(--)$ charge state results have been scaled by the factors indicated for clarity.

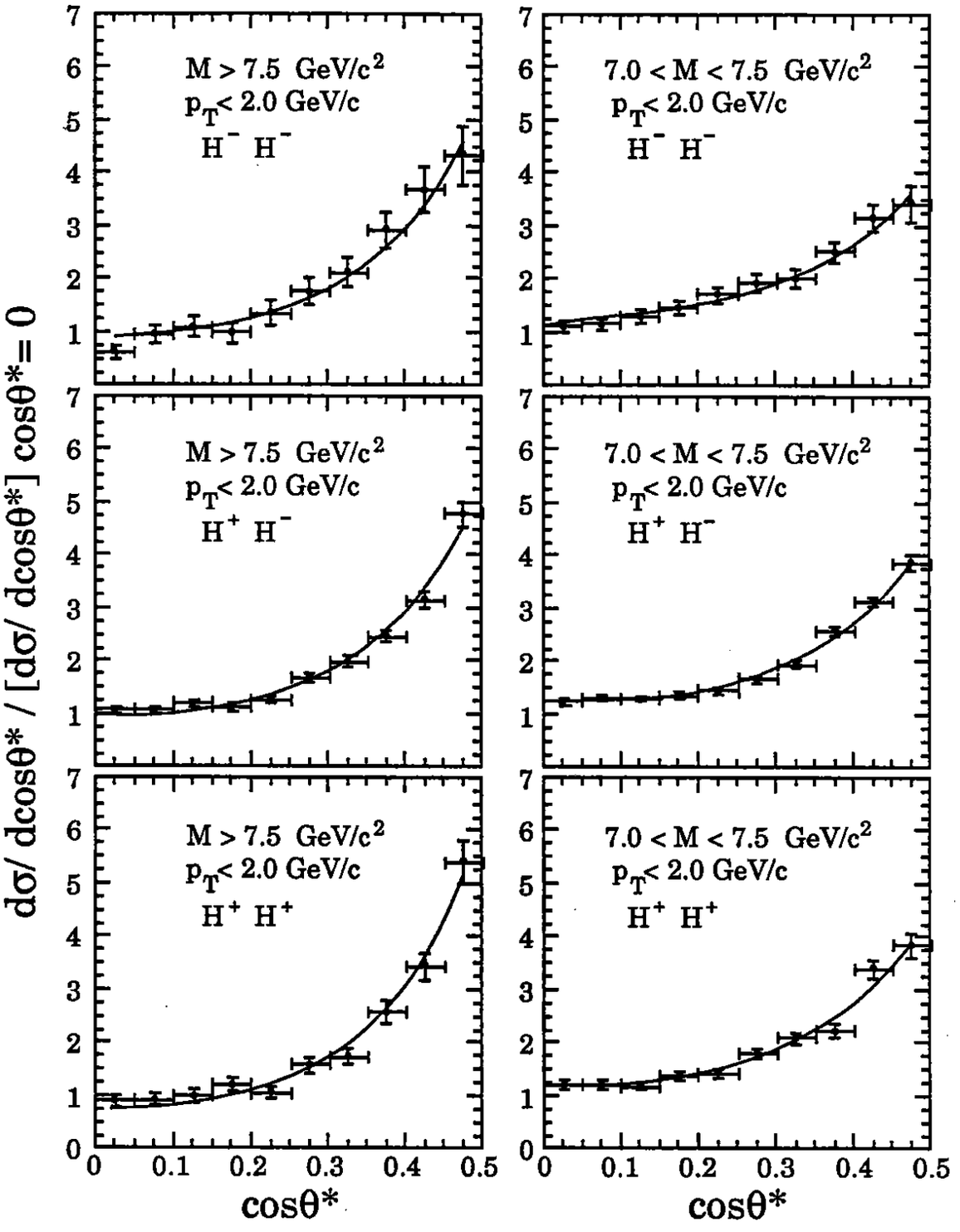

Fig. 7. The dihadron angular distributions as a function of cos0* for fixed mass bins using the combined data of the four targets. The curves shown are a functional fit to the normalized data. The errors indicated are statistical errors only.

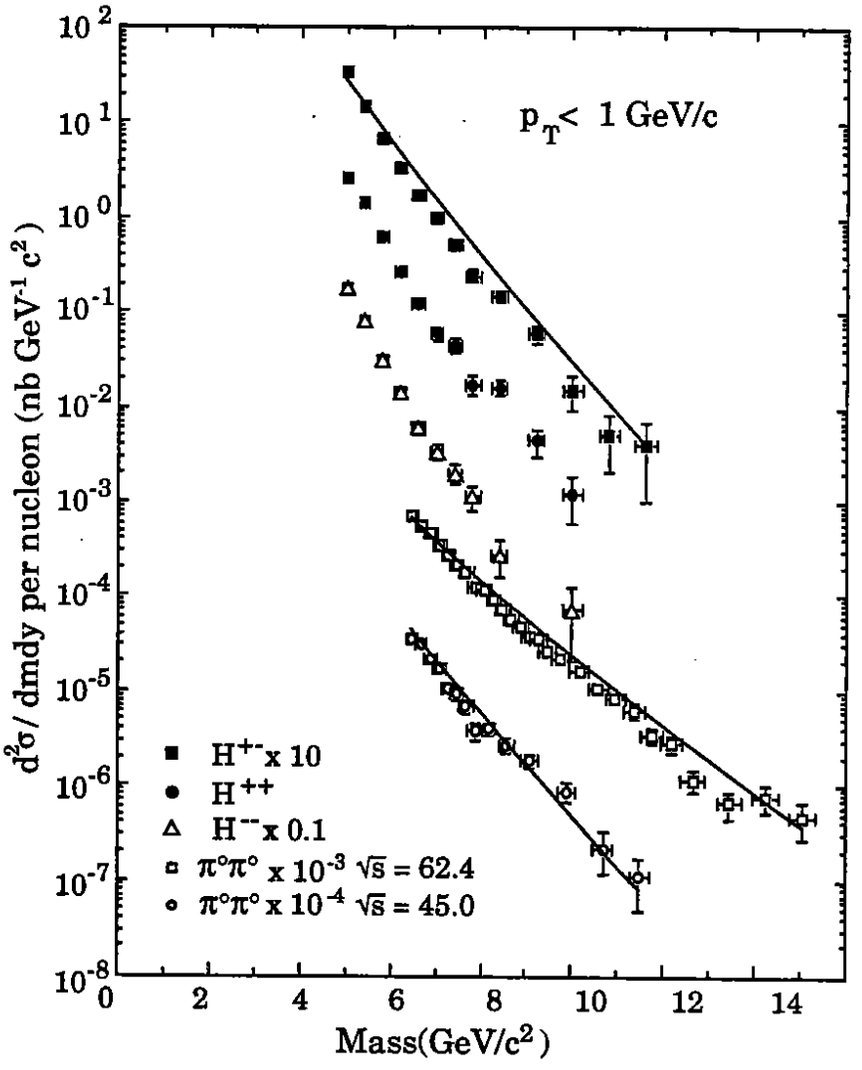

Fig. 8. The differential mass cross section dihadrons is plotted for $p_T < 1$ GeV/c. H^+ and H^- refer to positive and negative hadrons. The $(+-)$ charge state results, the $(--)$ charge state results and the CCOR neutral pion results have been scaled by the factors indicated for clarity. The curve is the CCOR function.

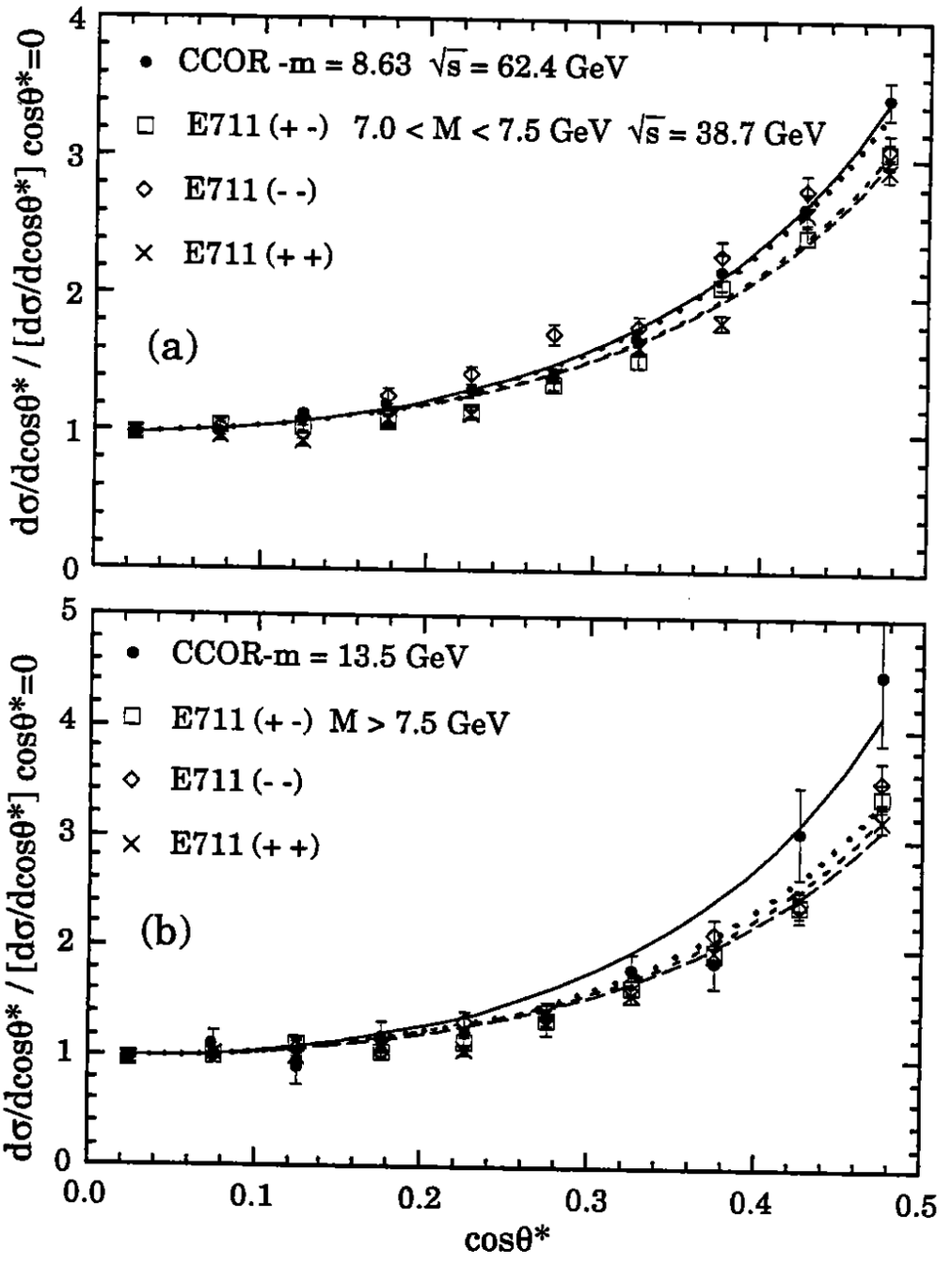

Fig. 9. The dihadron angular distributions for the three charge states and the two mass ranges of this experiment, and the neutral dipion data from the CCOR experiment. The curves correspond to a functional fit to the normalized cross sections.